5.1 Introduction

The Ruddlesdon D Popper (RP) phase defined by chemical formula $A_{n+1}B_nO_{3n+1}$,where n is an integer, for example, n=1 corresponds to A_2BO_4 and n=2 corresponds to $A_3B_2O_7$, etc. [167, 188]. The A_2BO_4 oxides can accommodate hyper stoichiometry oxygen at the interstitial oxygen sites between adjacent rock salt layer and perovskite and the resultant charge is compensated by the oxidation/reduction of transition metal (B) [118, 221]. The $A_2BO_{4+\delta}$ (where A = La^{3+}, Nd^{3+} or Pr^{3+} and B = $Cu^{2+/3+}$, $Ni^{2+/3+}$ or $Co^{2+/3+}$) based oxides exhibited as mixed ionic and electronic conductivity in temperature range 300-800^oC, which makes it a suitable candidate for cathode in intermediate-temperature solid oxide fuel cell (IT-SOFC) [162, 222]. The $La_2NiO_{4+\delta}$ have been extensively studied for electrolyte application in IT-SOFC due to their high oxygen ion conductivity [105, 223]. The change in oxygen stoichiometry in $La_2NiO_{4+\delta}$ can be achieved either by partial substitution of the alkaline earth metal (Sr, Ba, Ca) at La site or doping with transition metals like Cu, Co, Fe at Ni site [110, 223–225].

Properties of La-doped on alkaline earth site of perovskite oxides, $MSnO_3$ (M= Ba, Sr and Ca) have been investigated widely for transparent conducting oxide, humidity sensor, electrode material for IT-SOFC [65, 226–230]. La-doped $SrSnO_3$ and $BaSnO_3$ have been used for various applications such as humidity sensor, transparent conducting oxides, proton conducting electrolyte in fuel cells, etc. [212, 231–233]. The interesting properties of La-doped perovskite stannates motivated us to synthesize and study the effect of La doping on the electrical and optical properties of layered perovskite Sr_2SnO_4 to explore its applications.

5.2 Results and Discussions

In the present discussion, the system $Sr_{2-x}La_xSnO_4$ is abbreviated as SSL and the compositions with x=0, 0.1, 0.2, 0.4, 0.8 and 1.0 of this system are abbreviated as SSL0,

SSL1, SSL2, SSL4, SSB6 and SSL10 respectively through the discussion of the results. The discussion of sample SSL0 has excluded because it already discussed in Chapter 3.

5.2.1 Phase Formation and Structural Characterization using XRD

Room temperature powder X-ray diffraction pattern of all the samples has been recorded and shown in Figure 5.1. All the observed peaks in XRD patterns are indexed using crystallographic open database COD-1539931 of Sr_2SnO_4 [173]. The absence of any extra peaks corresponding to starting materials or secondary phase confirmed the formation of single phase solid solution for all the compositions. All the doped samples crystallized in tetragonal structure with space group $I4/mmm$. The peaks present in the diffraction pattern of samples are intense, indicating good crystallinity of the synthesized powders.

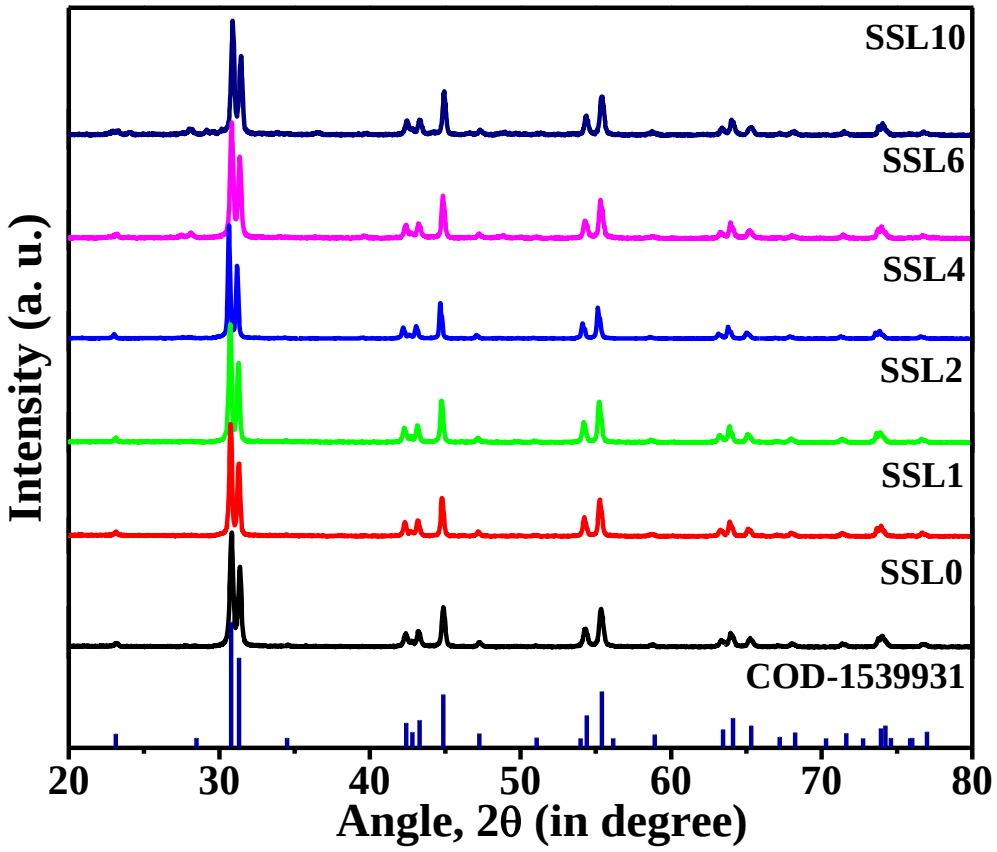

Figure 5.1 Room temperature powder X-ray diffraction pattern of all samples and theoretical XRD generated from COD database of Sr_2SnO_4.

To get detailed structural parameters of the synthesized samples the Rietveld refinement of the X-ray diffraction patterns are carried out using '**FullProf software suite**'. Pattern observed experimentally, calculated theoretically and their differences for all the samples are shown in Figure 5.2(a). The refinement process has already been described in Chapter 3. The structural parameters such as lattice parameter, unit cell volume, bond lengths, bond angles and other relevant parameters along with reliability factors R_p, R_{wp}, $R_{f,}$ and χ^2 are given in Table 5.1. The value of goodness of fit ($S = R_{wp}/R_p$) parameter is lying in between 1.02 – 1.22 reasonable for assigning the structure Sr_2SnO_4 for doped samples [239]. The structure obtained using **VESTA** software of the one representative sample SSL4 is shown in Figure 5.2(b). The crystal structure of all the synthesized samples remains tetragonal, while tetragonality (ratio of c/a), lattice parameters and cell volume is changing with the concentration of La (x).

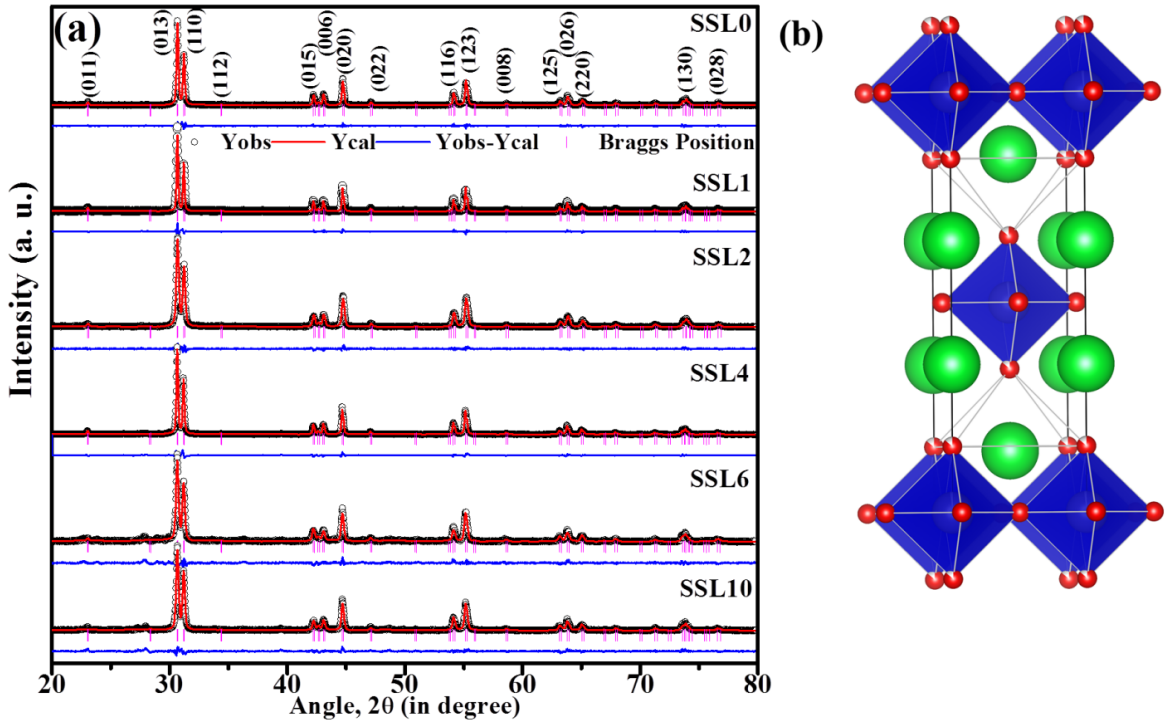

Figure 5.2 (a) The Rietveld refinement pattern of calcined powders. Here Yobs, Ycal, Yobs-Ycal and Braggs positions represent the experimental data, calculated data, the difference between both and Braggs position respectively. (b) Crystal structure of SSL4 obtained using VESTA software.

The variation of lattice parameters and degree of distortion R (=c/a) with the concentration of La (x) are shown in Figure 5.3(a) and 5.3(b), respectively. From Figure 5.3(a) it is observed that lattice parameters initially increases and attained maximum value for SSL4 and decreases on further increase of doping concentration (x). A similar trend of variation is observed for the cell volume (Table 5.1). The change in lattice parameters and cell volume with increasing La-concentration indicates that La has been incorporated at the Sr-site of Sr_2SnO_4. In the structure of Sr_2SnO_4 (as shown in Figure 5.2(b)) , the coordination number of Sr is 9 and the ionic radii of host ion Sr^{2+} and dopant ion La^{3+} in same coordination number is 1.31 Å and 1.21 Å, respectively. Based on the value of ionic radii, it is expected that lattice parameters should be decrease with increasing dopant concentration, but experimental result is opposite to the expectation. Similar experimental result have been reported in the literature for La, Sb-doped $BaSnO_3$ systems [235, 236]. In Sr_2SnO_4 structure, if La is substituted at Sr sites, it can occupy either sites of Sr present in perovskite $SrSnO_3$ or in SrO layers or distribute among both types of Sr sites. The solubility of La at Sr site in $SrSnO_3$ and Ba site in $BaSnO_3$ is very small up to ≤ 2 atom % [240], the higher solubility of La in layered perovskite Sr_2SnO_4 as compared to $SrSnO_3$ because the atomic packing fraction of Sr_2SnO_4 is lower than $SrSnO_3$ due to higher unit cell volume of Sr_2SnO_4 (Atomic Packing Fraction $\propto \frac{1}{Vol_{unit\ cell}}$). If the substitution of La takes place in the layer, an attractive force dominates between the Sn and La which results decrease in lattice parameters. Figure 5.3(b) shows the variation of degree of distortion with respect to composition of La, a decreasing trend in R is observed up to SSL4 and then becomes almost constant for composition SSL6 and SSL10. The reason for the initial decrease in R is that initially the increment in the value of lattice parameter **c** is smaller than the increment in the value of lattice parameter **a** thereafter, both the variation is seems to be almost equivalent which results almost constant

behaviour. In order to understand the effect of La doping on structure, numerical values of bond length and bond angles have been obtained from the refinement and given in Table 5.1.

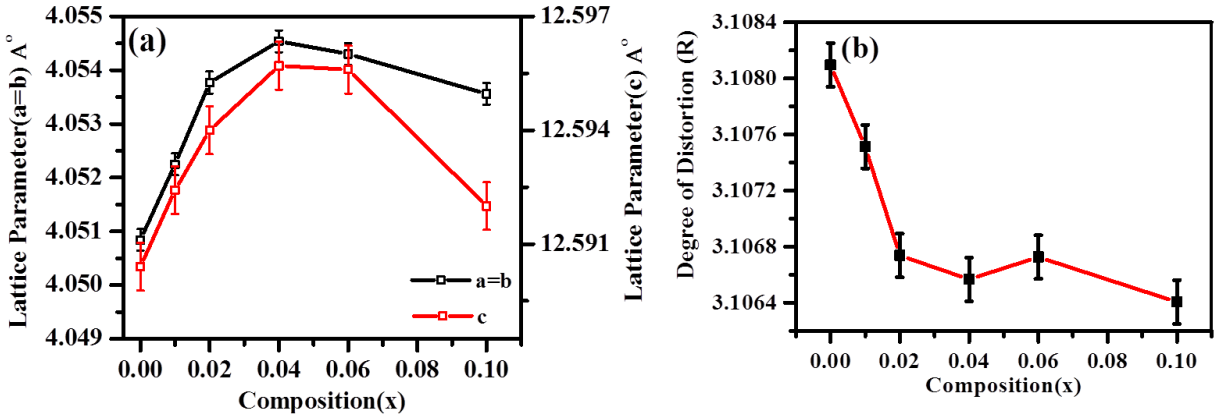

Figure 5.3 Variation of (a) Degree of distortion (R) and (b) lattice parameters with composition of La (x).

The broadening in the XRD peaks occurred on account of small crystallite size, instrumental broadening, lattice strain etc. The crystallite size of all the samples is calculated after exclusion of instrumental broadening using Eq. (2.15) [as described in Chapter 3 & 4] are listed in Table 5.2. It is observed from Table 5.2 that the crystallite size of doped samples is smaller than the undoped sample. The La^{3+} at the Sr^{2+} site of the Sr_2SnO_4 acts as a donor; it is reported in the literature that donor doping in perovskite oxides inhibits grain growth and hence results the smaller crystallite size of doped samples [221].

The crystallite size determined using Debye Scherrer's method have error due to broadening causes by lattice strain (microstrain). Therefore, in order to remove the contribution of microstrain, Size-Strain Plot (SSP) method has been used. Detailed procedure of determining crystallite size has been described in Chapter 2 using Eq. (2.19) [242]. According to the Eq. (2.19), plots of $\left(\frac{d_{hkl}\beta cos\theta}{\lambda}\right)^2$ vs. $\left(\frac{{d_{hkl}}^2\beta cos\theta}{\lambda^2}\right)$ for all samples are shown in Figure 5.4(a)- (f). In this plot, value of the crystallite size is determined from the slope of the linear fitting of the data. The square root of the intercept on y-axis gives the value of

lattice strain. The obtained values of crystallite size and lattice strain for all the samples are given in Table 5.2. From Table 5.2, it is noticed that the value of crystallite size obtained using SSP plot is slightly higher than the value obtained using Debye Scherrer formula. The difference clearly reflects the presence of lattice strain in the samples. Further, it is observed that the value of lattice strain for all the La-doped samples is higher than undoped sample. The higher value of lattice strain observed for doped samples is may be due to smaller ionic radii of the La^{3+} than Sr^{2+} ion.

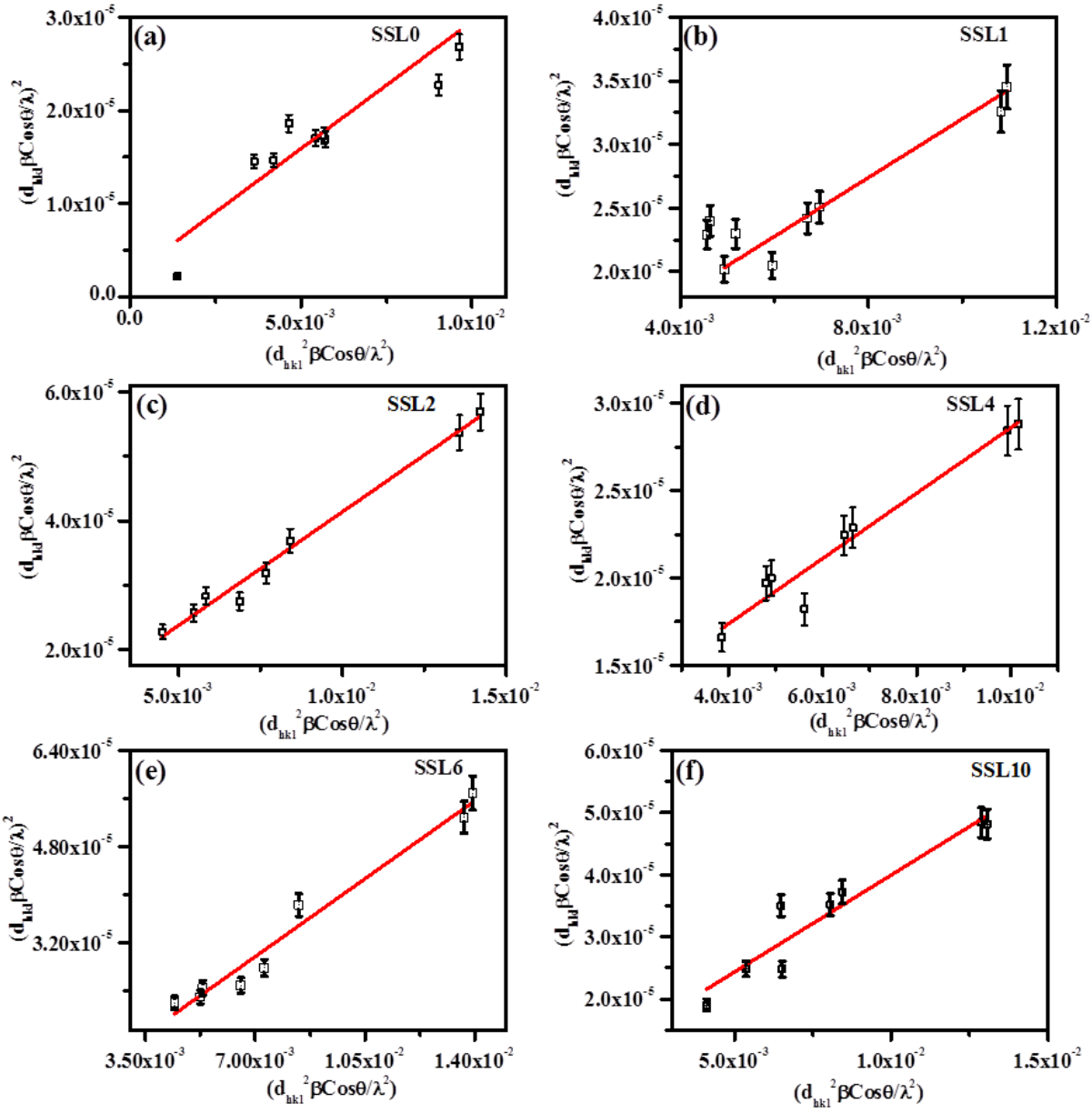

Figure 5.4 Size-strain plots (SSP) for the determination of crystallite size and lattice strain.

Table 5.1 Structural parameters obtained from the Rietveld refinement of XRD pattern of the samples.

Sample/Code	**Sr_2SnO_4 (SSL0)**	**$Sr_{1.99}La_{0.01}SnO_4$ (SSL1)**	**$Sr_{1.98}La_{0.02}SnO_4$ (SSL2)**	**$Sr_{1.96}La_{0.04}SnO_4$ (SSL4)**	**$Sr_{1.94}La_{0.06}SnO_4$ (SSL6)**	**$Sr_{1.90}La_{0.10}SnO_4$ (SSL10)**
Space group	I4/mmm	I4/mmm	I4/mmm	I4/mmm	I4/mmm	I4/mmm
Lattice parameters (Å) a=b c	4.05084(6) 12.59040(18)	4.05225(5) 12.59240(14)	4.05377(7) 12.5940(14)	4.05454(5) 12.59570(12)	4.05430(3) 12.59560(11)	4.05356(6) 12.59200(11)
Tetragonality (R = c/a)	3.1080	3.1075	3.1067	3.1065	3.1068	3.1064
Cell Volume ($Å^3$)	206.60	206.78	206.94	207.06	207.04	206.90
Uiso	0.84	0.82	0.83	0.86	0.89	0.91
La on 4e (0,0,0.3527)		4.05225(4)	4.04977(5)	4.05454(5)	4.0543(3)	4.05356(11)
Uiso	--	0.87	0.85	0.81	0.83	0.94
Sn on 2a(0,0,0)	3.412551(18)	3.40992(2)	3.41409(4)	3.41578(3)	3.3976(15)	3.41497(7)
Uiso	0.82	0.84	0.83	0.89	0.87	0.93
O1 on 4c (0.5,0,0)	4.88039(20)	4.88740(6)	4.87607(13)	4.88183(6)	4.8859(3)	4.88032(19)
Uiso	1.18	1.24	1.45	1.34	1.38	1.31
O2 on 4e(0,0,0.1527)	2.74648(8)	2.74270(2)	2.74879(5)	2.74914(3)	2.7266(15)	2.74849(7)
Uiso	1.08	1.04	1.16	1.05	1.09	1.07
Selected Bond lengths (Å)						
Sn-Sr/La (within perovskite)	3.41255(3)	3.41392(6)	3.41409(5)	3.41578(8)	3.39765(4)	3.41297(2)
Sn-O2(within perovskite)	1.98349(4)	2.03229(7)	2.04795(3)	2.06378(6)	2.05409(9)	2.01978(5)
Sr-O2(out of perovskite)	2.45677(6)	2.41535(8)	2.34780(7)	2.31462(5)	2.36370(5)	2.34798(3)
Selected Bond Angles (in degree)						
O2-Sr-O2(within perovskite)	89.884(3)	89.765(6)	89.636(2)	89.545(4)	89.632(5)	89.716(2)
O2-Sn-Sr(within perovskite)	122.927(7)	122.828(5)	122.790(8)	122.730(7)	122.960(9)	122.930(4)
O2-Sr-O2 (in layer)	174.860(7)	172.660(5)	170.850(8)	168.570(7)	170.610(9)	174.030(4)
χ^2	4.17	4.07	5.05	5.16	6.42	8.76
R_p	16.7	11.9	13.7	13.9	25.9	23.2
R_{wp}	20.4	12.6	16.5	14.0	28.1	26.3
R_{Bragg}	3.43270	2.53210	3.15420	3.96978	7.26205	6.59891
Goodness of fit ($S=R_{wp}/R_p$)	1.22	1.06	1.20	1.01	1.08	1.13

5.2.2 Transmission Electron Microscope (TEM) Analysis

The particle size of the synthesized samples has been determined by transmission electron microscopy (TEM). The bright field image of a representative sample SSL4 is shown in Figure 5.5. The morphology reflects spherical shape of particles. The particle size is determined using "**Image J**" software. The average particle size is determined by fitting Gaussian function to the histogram of distribution of particle size. The average particle size of the sample is found to be (37.50 ± 2.50) nm. The selected area electron diffraction (SAED) pattern as shown in Figure 5.5(c) consists of regular ring pattern with bright spot typical nature of polycrystalline sample. These rings pattern corresponds to Miller planes (hkl) of unit cell of Sr_2SnO_4. The planes with their Miller indices as indexed in Figure 5.5(c) are in agreement with XRD result.

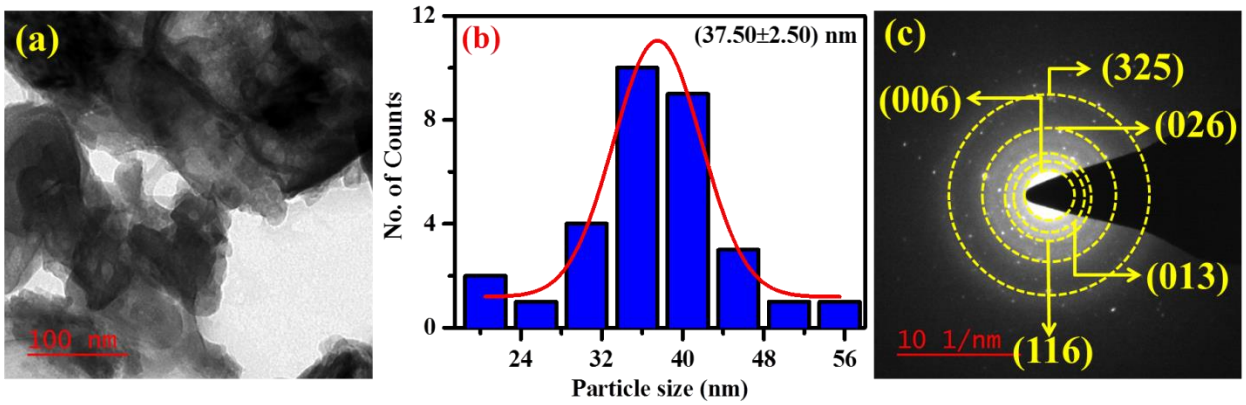

Figure 5.5 (a) Transmission electron micrograph of a representative sample SSL4, (b) Distribution function fitted with Gaussian Function and (c) Selected Area Electron Diffraction (SAED) pattern.

5.2.3 Raman Spectrum Analysis

The Raman spectroscopy is a simple and non-destructive tool to probe structural information at single unit cell level. In this work, Raman technique has been used to study the incorporation of La^{3+} ions at Sr-site of Sr_2SnO_4 and to detect the impurity phase present in

trace amount. As it is mentioned that the Sr_2SnO_4 synthesized in this work crystallized in tetragonal structure with symmetry group D_{4h}^{17} and space group ($I4/mmm$) [243]. The theoretical mode analysis according to group theory for tetragonal crystal structure and space group $I4/mmm$ predicts 14 bands which are given below;

$$\Gamma_{optic} = 2A_{1g} + 2E_g + 4A_{2u} + 5E_u + B_{2u} \quad (5.1)$$

Out of these 14 modes only four modes are Raman active. Figure 5.6 illustrates the room temperature Raman spectrum of the samples in the wavenumber range from 100-1000 cm^{-1}. In Raman spectrum of Sr_2SnO_4, it is noticed that the band has splitted into two bands one at 561 cm^{-1} and another at 581 cm^{-1}. The splitting of the A_{1g} band in Sr_2SnO_4 is attributed to the difference in bond length of Sn-O bond parallel to the layer and perpendicular to the layer (parallel and parallel to c-axis). On initial substitution of La^{3+} at the site of Sr^{2+} the position of these bands moved towards higher wavenumber side due to the heavier (57 %) atomic mass of La than Sr. Furthermore, it is noticed that with increasing doping concentration of La the spacing between the modes decreases and finally merged into a single band for SSL4 sample which may be due to almost equal value of bond Sn-O2 (2.0727) to Sn-O1 (2.0637). However, for higher doping concentrations (x=0.06 and 0.10), i.e., for samples SSL6 and SSL10 Raman spectrum again splits into two bands similar to undoped sample SSL0. The change in the position and shape of the bands for doped samples confirms the substitution of La at Sr site of Sr_2SnO_4. Absence of bands corresponding to starting materials La_2O_3 (250, 350, 440 cm^{-1}), $SrCO_3$ (412 and 592 cm^{-1}), SnO_2 (472 and 632 cm^{-1}), or any other secondary phase such as $SrSnO_3$, confirms the purity of the synthesized samples at the local level [239, 240].

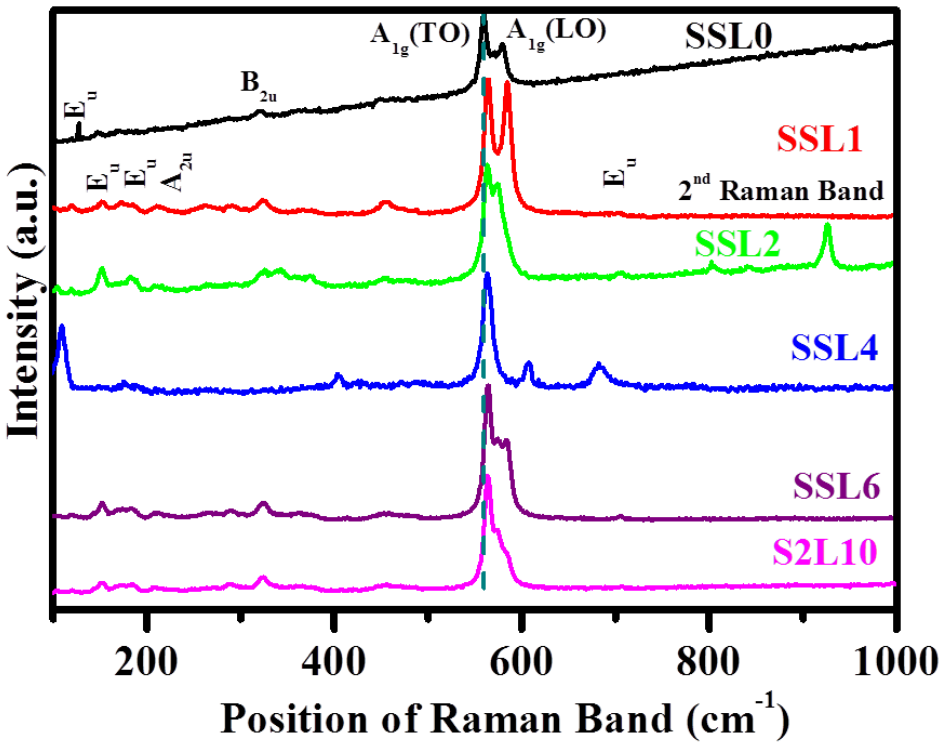

Figure 5.6 Room temperature Raman spectrum of the prepared samples.

5.2.4 Fourier Transform Infrared Spectroscopy (FTIR) analysis

Fourier transform Infrared (FTIR) technique has been employed to study the presence of various functional groups and the changes in vibrational bands due to incorporation of La^{3+} at Sr^{2+} site of Sr_2SnO_4. FTIR spectrum of the synthesized powders has been recorded in the range of 400 -4000 cm^{-1} and depicted in Figure 5.7(a). The FTIR spectrum of Sr_2SnO_4 contains two characteristic bands corresponding to Sr-O and SnO_6 observed at 502 cm^{-1} and 726 cm^{-1}, respectively. Doping of La either Sr or Sn or simultaneously on both sites may bring change in the positions, shape as well as the intensity of these characteristic bands [176, 199]. The magnified view of bands observed at 502 cm^{-1} and 726 cm^{-1} is shown in Figure 5.7(b). It is noticed that the position of band corresponding to Sr-O vibration shifted approximately 10-12 cm^{-1} towards higher wavenumber side for doped samples which may be due to higher atomic mass of La compared to Sr. On the other hand, the band observed at 702 cm^{-1} corresponding to stretching mode of SnO_6 is not shown any significant shift with doping

concentration. Therefore, the variation in the shape, position, and the intensity of peak indicates the incorporation of La takes place into the lattice of Sr_2SnO_4.

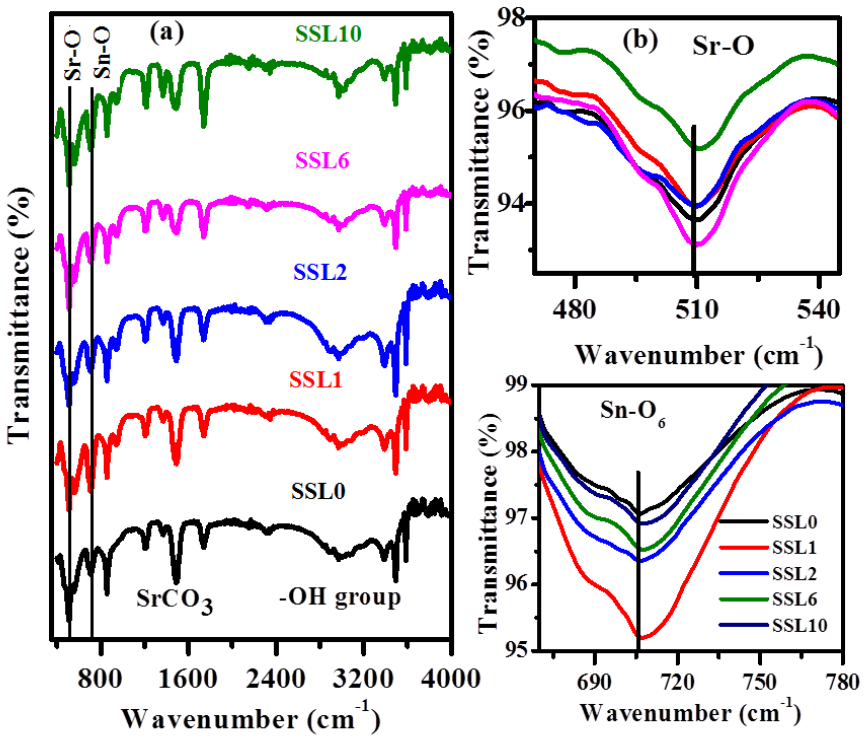

Figure 5.7 (a) Room temperature Fourier transform infrared (FTIR) spectrum of the sample (b) Enlarge view of band corresponding to stretching mode of Sr-O and $Sn-O_6$.

5.2.5 Microstructural study using FESEM

FE-SEM is used to study the morphology of the fractured surface of sintered ceramic samples. All micrographs are recorded at the same magnification and displayed in Figure 5.8. The microstructure of samples is looking like dense and grains are spherical in shape. The Histogram for each sample is generated for spherical grains using "**Image J**" software. Further the average grain size is determined by fitting of Gaussian distribution function and shown in Figure 5.9.

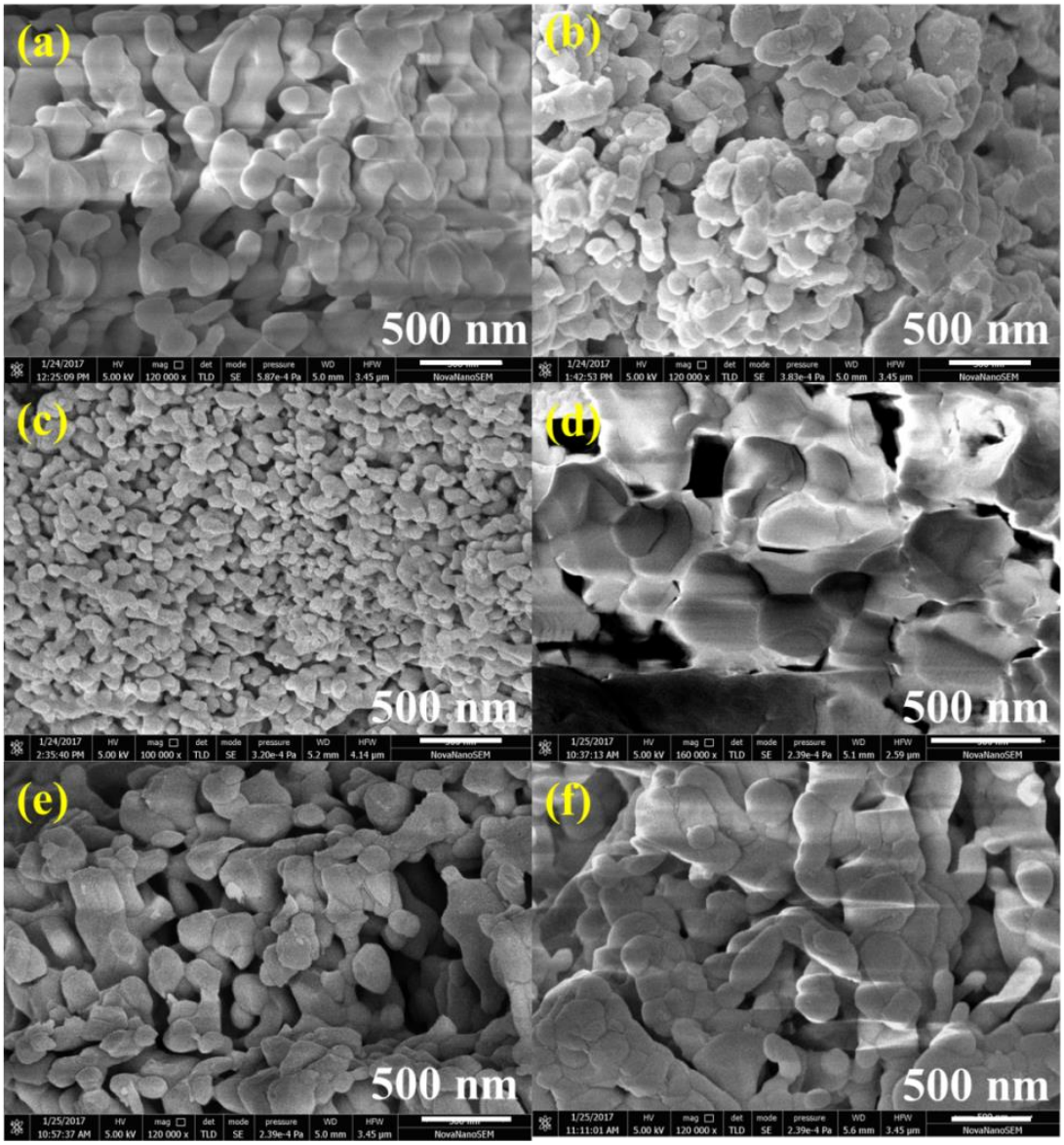

Figure 5.8 Scanning electron micrograph of the fracture surface of sintered sample (a) SSL0 (b) SSL1 (c) SSL2 (d) SSL4 (e) SSL6 (f) SSL10.

The average grain size of samples is found to be in the range of (184±20) nm to (210±22) nm. Initially, the grain size decreases from SSL0 to SSL4 and then increased for SSL6 and SSL10. This variation could be discussed in further sections.

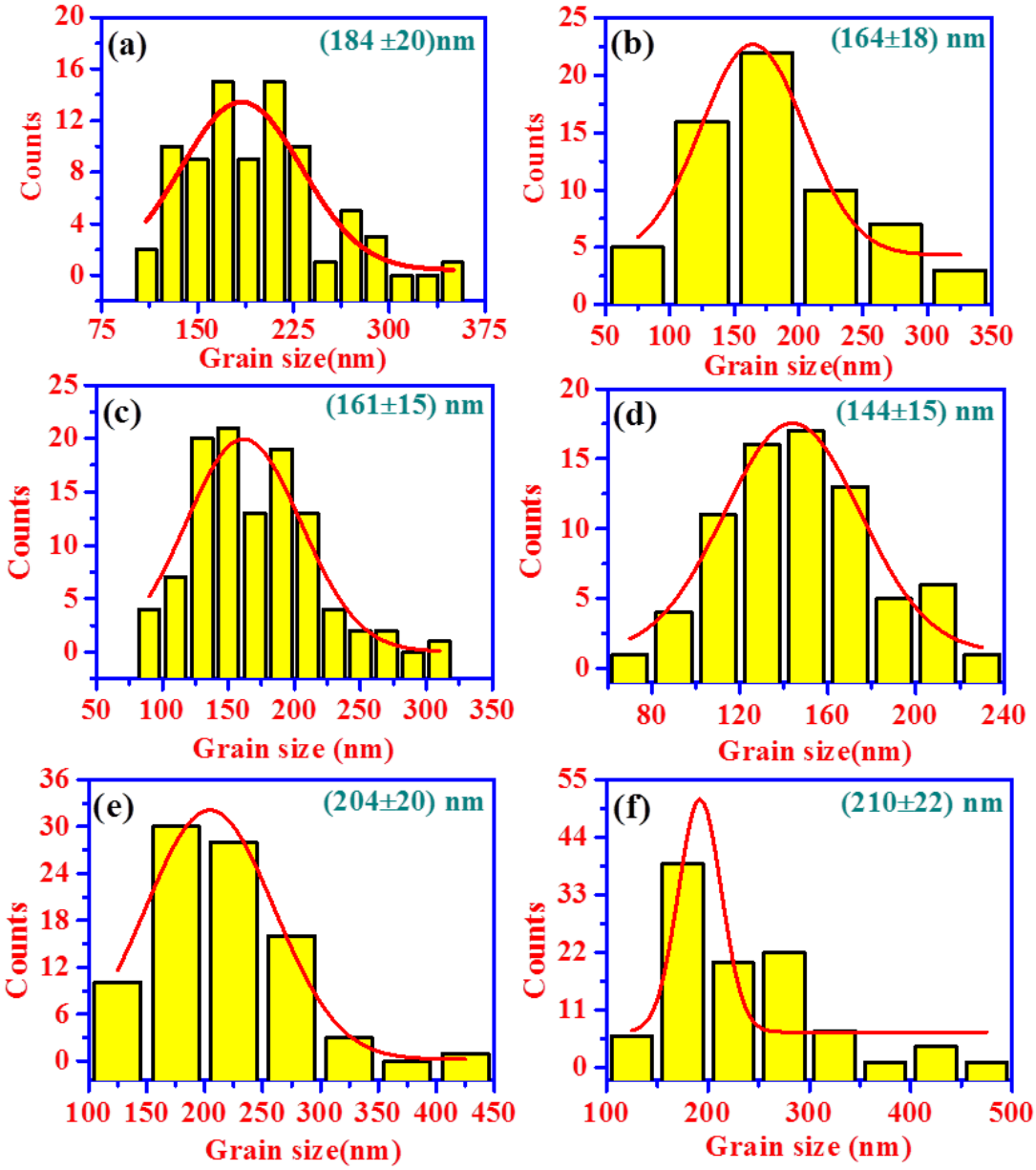

Figure 5.9 Histogram between no. of grains and grain size (a) SSL0 (b) SSL1 (c) SSL2 (d) SSL4 (e) SSL6 (f) SSL10.

5.2.6 X-ray Photoelectron Spectroscopy (XPS) analysis

The X - ray photoelectron spectroscopic technique is used to reveal the valence state of the constituent elements present in the composition SSL4. Figure 5.10 (a) shows the survey scan report of the sample. The XPS spectra corrected with respect to C 1s are appeared at 284 eV. Based on the literature peaks observed at 133, 284, 484.8, 529.6 and 835 eV corresponding to chemical state of Sr 3d, C 1s, Sn 3d, O 1s and La 3d, respectively [246]. Further, valance

state of these elements is determined using high resolution XPS spectra (HRXPS). Figure 5.9(b) depicts the HRXPS spectra for Sr 3d. Two peaks positioned at 132.95 eV and at 134.70 eV have been fitted to core level spectra of Sr 3d for Sr $3d_{5/2}$ and Sr $3d_{3/2}$ respectively. The separation between these peaks is 1.75 eV, indicates existence of Sr in Sr^{2+} state[216]. The core level XPS spectra of La 3d depicted in Figure 5.10(c) shows a doublet peaks at 834.65 and 838.30 eV. The position of this peak is compare with literature report and belongs to state La $3d_{5/2}$. The energy of separation between these peaks is 3.65 eV, which means that La is present in La^{3+} state [247]. Figure 5.10(d) shows the spectrum of the core level of Sn 3d, two peaks corresponds to $3d_{5/2}$ and $3d_{3/2}$ are observed at 486.25 eV and 494.65 eV at [178, 212]. In both the peak, the energy of separation between these peaks is 8.4 eV, indicating the presence of Sn [218]. These peaks have been deconvoluted into two peaks as shown in Figure 5.10(d). The broadening of peak with slight asymmetry towards lower binding energy side may be associated with multivalancy of Sn. The position of these peaks in $3d_{5/2}$ state is 485.85 eV and 486.30 eV, while in $3d_{3/2}$ is 494.25 eV and 494.70 eV respectively. The peak observed at lower binding energy is assigned to Sn^{2+} and higher binding energy to Sn^{4+}. The core level spectra of O 1s shown in Figure 5.10(e) represent a single peak at 531.1eV. The asymmetry in the peak towards lower and higher binding energy side indicates the presence of different types of oxygen species. This peak is deconvoluted into three peaks having positioned at 530.2 eV, 531.1 eV and 531.8 eV respectively. The peak at 530.2 eV is assigned as interstitial oxygen, 531.1 eV is associated with O^{2-} i.e. lattice oxygen, while the peak at 531.8 eV is attributed to oxygen vacancies [248].

The presence of defects can be easily understood by Kronger-Vink notation of defect. In present work the sample is synthesize at high temperature and slow diffusion process, therefore possibility of oxygen loss may take place according to Eq. (1.10) and reduction of Sn^{4+} into Sn^{2+} according to Eq. (3.5).

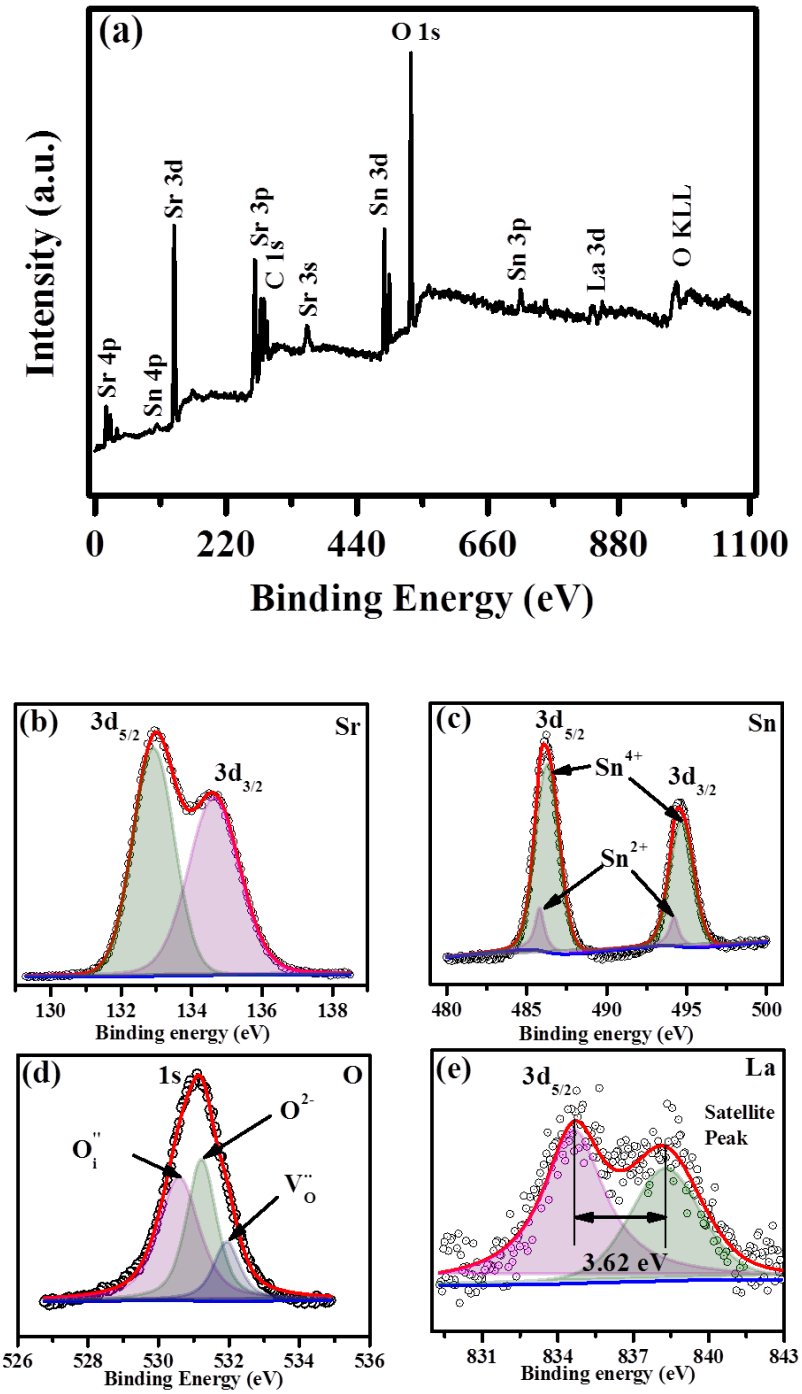

Figure 5.10 (a) Survey scan report of SSL4 (b-e) Core level spectra of Sr (3d), La (3d), Sn (3d) and O (1s) spectra.

5.2.7 UV-Visible Spectroscopy

The Ultraviolet-visible (UV) spectroscopy technique has been used to investigate the optical absorbance of the undoped Sr_2SnO_4 and La-doped Sr_2SnO_4. The room temperature

UV spectrum of the samples recorded in the wavelength range 200-800 nm is shown in Figure 5.11. The absorbance edge wavelength has been determined by extrapolation of linear region on the X-axis (as shown in the inset of Figure 5.11). It is observed that the absorbance edge systematically shift towards the higher wavelength side (≈ 15 nm) with increasing the dopant concentration of La. It is further noticed that in the UV spectrum of doped samples, a hump is present in wavelength range 300-350 nm which may arise due to the electronic transition from d to f shell of La^{3+}. Further, it is observed that with increasing dopant concentration the position of hump moves towards the visible region (upto 500 nm) for SSL4 which shows the incorporation of La into the lattice of Sr_2SnO_4 [212].

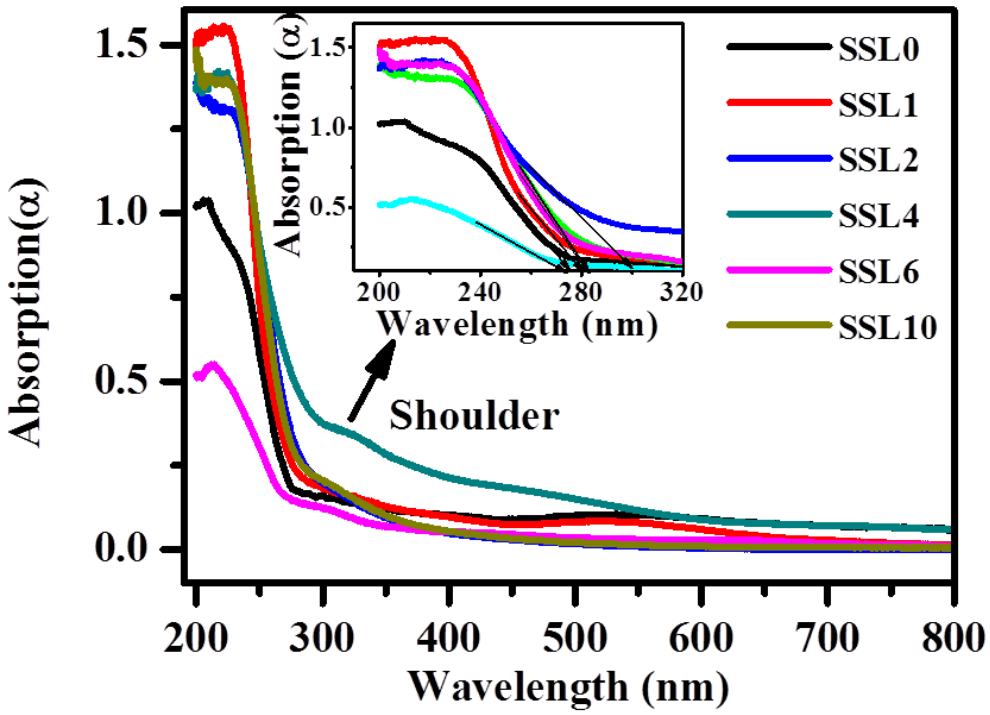

Figure 5.11 Room temperature UV-Visible absorption spectrum of the prepared samples.

The La^{3+} at the Sr^{2+} site in Sr_2SnO_4 behaves as a donor, and its energy levels lie just below the conduction band. The position of donor level moves towards conduction band on increasing the concentration of La in solid solution. This donor can act as trapping level for the electrons which may bring a shift in the position of absorbance edge towards visible

region. In the literature, similar results have been reported on lanthanide doped ZnO, La-doped perovskite [244, 245]. The optical band gap of the samples is determined using Eq. (2.21) for both the values of index parameter $m = 1/2$ and 2 are shown in Figure 5.12. The optical band gap (both direct and indirect) has been determined through the intercept of linear region in the Tauc plot on x-axis (Energy), where y=0. The value of energy for both the band gap obtained using this method is indexed in Table 5.2. From Table 5.2 it is noticed that energy value of direct band gap is increases with increase in the dopant concentration of La upto SSL4 thereafter, it decreases on further increase in the dopant concentration for SSL6 and SSL10. It is known that La^{3+} at the Sr^{2+} site is a donor and charge compensation mechanism can be takes place according to following equation;

$$La_2O_3 \xrightarrow{Sr_2SnO_4} 2La_{Sr}^{\cdot} + 2e' + 3O_0{}^{x} \qquad (5.2)$$

The donor level $(La_{Sr}^{\cdot})$ lies below the conduction band, compensated by creation of electron as shown by Eq. (5.1). Then a repulsive force acts between donor level and conduction band which may be responsible for increase the band gap upto SSL4. On further increase in the dopant concentration of La (for compositions SSL6 and SSL10), the donor level shifts towards conduction band. Therefore, it is possible that the donor levels and conduction band has overlap together to form a continuous band and results a decrease in the band gap. Similar findings have been reported on other donor doped oxide materials [251, 252].

It is inferred from Table 5.2 that value of indirect band gap is lower than the value of direct band gap for the same composition. The lower value of indirect band gap may be due to the presence of defects such as oxygen vacancies (V_o^x, $V_o^{\bullet}$ and $V_o^{\bullet\bullet}$), lattice defects and distortion in local bond. Among the various defects mentioned the most commonly found defects in oxides materials are oxygen vacancies (V_o^x, $V_o^{\bullet}$ and $V_o^{\bullet\bullet}$) which are found from the XPS analysis of the sample. Furthermore, it is noticed that the value of the indirect band gap

(see Table 5.2) decreases with increasing dopant concentration (x) upto SSL4 and slightly increases for the composition SSL6 and SSL10. M. Ganguly et al. had investigated the effect of La doping at the site of Ba in $BaTiO_3$, and they found similar results [212].

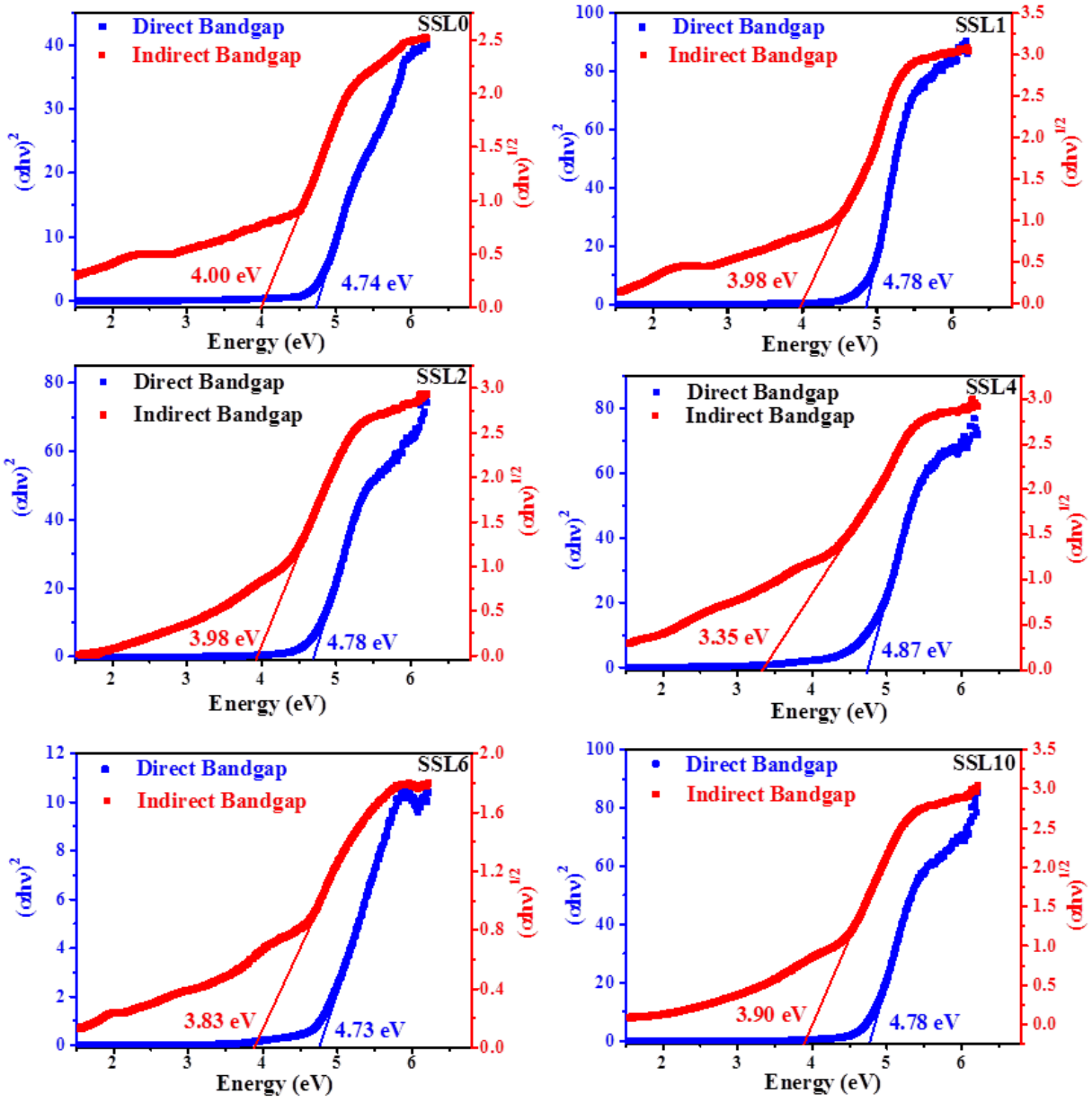

Figure 5.12 Tauc plot (by putting m=1/2 for direct band gap and m=2 for indirect band gap) obtained from absorption data of the samples.

Table 5.2 Crystallite size and lattice strain obtained from Size-Strain plot (SSP) and optical bandgap from Tauc plot of the samples.

S.No	Sample code	Crystallite Size (nm) obtained from		Strain(ε) x 10^{-3}	Optical Band gap (eV)	
		Debye-Scherer method	SSP plot method		Direct Bandgap	Indirect Bandgap
1.	SSL0	49.3	51.2	3.00	4.74	4.00
2.	SSL1	37.6	39.4	5.95	4.78	3.98
3.	SSL2	32.4	31.8	5.98	4.81	3.84
4.	SSL4	30.8	30.5	6.27	4.87	3.35
5.	SSL6	31.6	33.2	5.90	4.73	3.83
6.	SSL10	34.2	35.8	5.45	4.78	3.90

5.2.8 Electrical Characterization

5.2.8.1 AC conductivity analysis

AC conductivity of all the compositions has been measured in temperature range (60-600) ^{o}C and frequency range (20 Hz – 2 MHz). The variation of AC conductivity with frequency at few temperatures for sample SSL4 is shown in Figure 5.13(a). The other compositions of other SSL system show more or less with the same conductivity behaviour as a function of frequency. The total conductivity as shown in Figure 5.13(a) is the combination of two distinct regions; the first region is the frequency independent plateau termed as dc conductivity (σ_{dc}) and the second region is the frequency dependent in which the conductivity increases linearly with frequency termed as ac conductivity (σ_{ac}). Thus the total conductivity at particular frequency and temperature follows Johnscher's power law given by Eq. (2.36). Three parameters σ_{dc}, f_H, and n are obtained by fitting of Eq. (2.36) to the conductivity shown in Figure 5.13(a). In this Figure symbols represents experimental data whereas solid line is fitting curve.

In order to study dc conduction mechanism in the samples, temperature dependent behaviour of σ_{dc} has been studied. The variation of dc conductivity ($\log \sigma_{dc}$) with inverse temperature (1000/T) for all samples is shown in Figure 5.13(b). Two linear regions with different slope

have been observed in $\log \sigma_{dc}$ vs. 1000/T plot for all the samples. These regions are marked as 1 and 2 in Figure 5.13(b). Value of the activation energy $E_{cond.}$ is determined by linear fitting of Eq. (3.10) to dc conductivity data in both the regions are given in Table 5.3. Further, the logarithmic of hopping frequency with respect to inverse of temperature (1000/T) is shown in Figure 5.13(c) for all samples, which shows a straight line $[(y = mx + c), y = \log_{10} f_H, x = \frac{1000}{T}, m = \left(-\frac{E_{ac}}{1000k}\right), c = \log f_o]$ indicated Arrhenius type relation. Two regions similar to dc conduction are found, and the value of activation energy determined using the value of the slope is given in Table 5.3. In order to see the correlation between dc and ac conduction, the logarithmic of dc conductivity with respect to logarithmic of hopping frequency is plotted in Figure 5.13 (d). A linear trend with unit slope indicated that both the conduction ac as well as dc are occurred by the similar processes.

From Table 5.3, it is found that the activation energy obtained from hopping frequency is almost equivalent to the activation energy obtained from dc conductivity. The activation energy for dc conduction $E_{cond.}$ is found to be in the range (0.50-0.23) eV in region 1 and (0.10-0.16) eV in region 2 respectively, while for hopping frequency E_{ac} it is found to be in range of (0.21-0.50) eV in region 1 and (0.12-0.16) eV in region 2 respectively.

As it is observed that the activation energy obtained from dc conductivity and hopping frequency is almost same. However, in undoped sample SSL0, only a single conduction mechanism is operative while two regions are operative in La-doped samples. To understand this variation and conduction mechanism the XPS spectra of sample SSL0 (Section 3.2.6) and SSL4 (Section 5.2.6) is compared. On comparison it is found that both the sample shows the presence of oxygen vacancies, however additional interstitial oxygen vacancy is observed for SSL4 sample. In present case, the substitution of La at Sr-site is hetrovalent type and the charge compensation takes place by following manners.

$$La_2O_3 \xrightarrow{2SrO} 2La_{Sr}^{\cdot} + 2e' + 2O_O^x + \frac{1}{2}O_2 \quad (5.3)$$

$$Sn_{Sn}^x + 2e' \rightarrow Sn_{Sn}'' \quad (5.4)$$

$$La_2O_3 \xrightarrow{2SrO} 2La_{Sr}^{\cdot} + O_i'' + 2O_O^x \quad (5.5)$$

$$La_2O_3 \xrightarrow{2SrO} 2La_{Sr}^{\cdot} + V_{Sr}'' + 2O_O^x + \frac{1}{2}O_2 \quad (5.6)$$

The activation energy observed in region 2 for La-doped samples is almost same to activation energy of SSL0, which indicates that the conduction in doped samples of region 2 is governed by transfer of electron between the sites of Sn^{4+}/Sn^{2+}. Moreover, the higher value of activation energy (0.21-0.50) eV in region 1 suggests migration of oxygen interstitial along a and b directions of Sr_2SnO_4 (according to Eq.5.4)) [253]. As it is found that with increasing La there is decrease in activation energy which suggests that migration of oxygen interstitial takes place along a, b plane.

In order to know the role of La, the value of dc conductivity at 400^{o}C is plotted with respect to composition of La in Figure 5.14(a). The value of σ_{dc} was 7.11 x 10^{-6} S-cm^{-1} for SSL0 increased with incorporation of La upto 7.28 x 10^{-5} for SSL4 and then decreased for SSL6 to 2.30 x 10^{-5} and 9.20 x 10^{-6} for SSL10. From Eq. (5.2), the extra charge created by La substitution might be compensated by partially Eq. (5.2) and (5.4) which indicates increase in oxygen interstitial results an increase of electron and hole in some way which is responsible for the higher electronic conductivities in the samples. Above than SSL4, the dc conductivity decreased which may be following possibility;

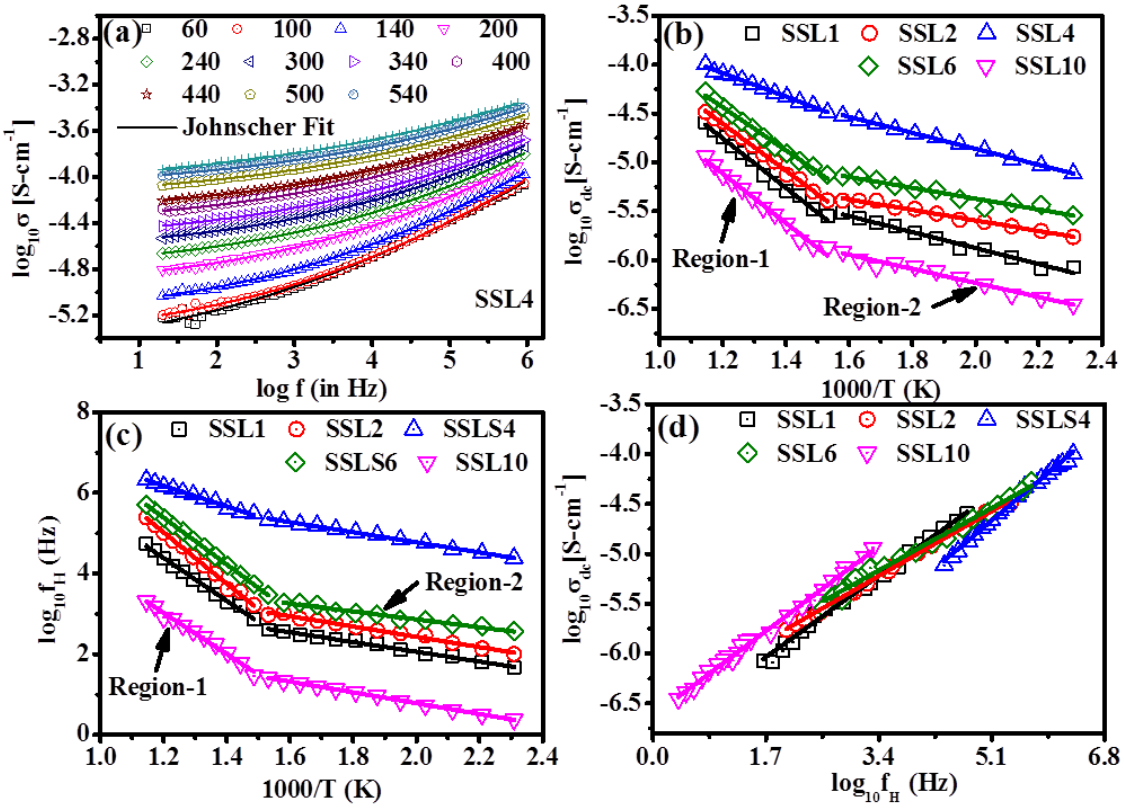

Figure 5.13 (a) Variation of AC conductivity with logarithmic of frequency, (b) Arrhenius plot generated for all sample using Eq. (13) (c) Arrhenius plot generated for all sample using hopping frequency (d) Variation of dc conductivity vs. hopping frequency for all sample.

First possibility is that for composition SSL6 and SSL10, there might be possibility that migration of interstitial oxygen takes place along the c-axis of Sr_2SnO_4 which is almost 3 times higher than the a=b axis. The migration along c-axis is slight difficult than a, b plane and results decrease in dc conductivity.

Second possibility is that for composition SSL6 and SSL10, there may be possibility that the charge compensation process takes place according to Eq. (5.6). Vacancies of Sr do not contribute significantly to the conduction because it requires higher thermal activation energy. Due to immobility of V_{Sr}'' within investigated temperature range it results decrease in dc conductivity.

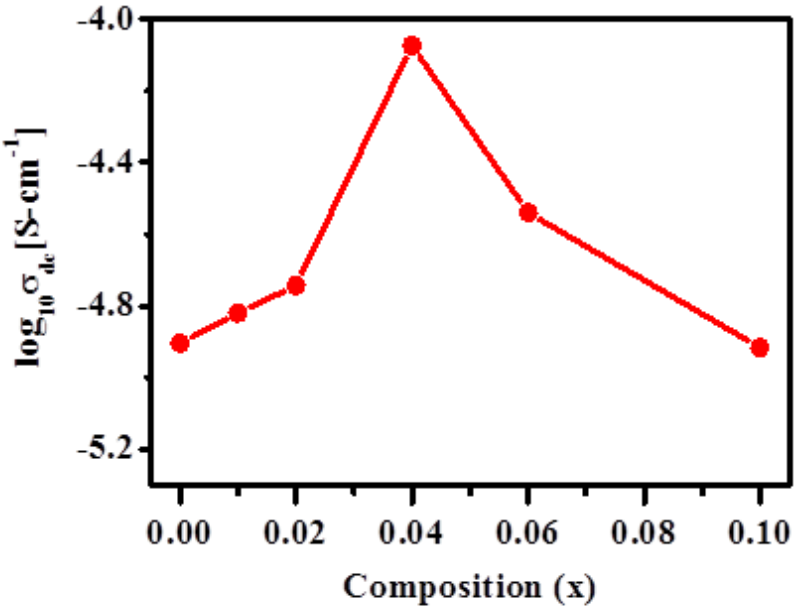

Figure 5.14 Variation of dc conductivity with composition of La (x) at 400^{o}C.

As discussed in Section 3.2.5.2, temperature dependent response of exponent (n) suggests the nature of ac conduction in the samples [189]. Figure 5.15(a) shows the variation of exponent (n) with temperature for all the compositions. Similar to undoped Sr_2SnO_4 and for doped samples exponent (n) is found temperature independent within the studied temperature range which shows that conduction in these samples are governed by Quantum mechanical tunnelling (QMT) of electrons between Sn^{2+} and Sn^{4+} sites. Presence of Sn^{2+} ions in doped samples has been confirmed from their XPS study discussed in Section 5.2.6. Further, variation of ac conductivity (σ_{ac}) at 10 KHz of all samples have been plotted against temperature are shown in Figures 5.15(b) to 5.15(f). By fitting of Eq. (3.11) to experimental data of AC conductivity according to QMT model are shown in Figure 5.15(b) to 5.15(f). The solid line shows best fit of to the experimental data points and the value of $\alpha, N(E_F)$ and R_ω are obtained and given in Table 5.3. The value of $N(E_F)$ is found to be increased for sample SSL1 to SSL4 and thereafter it decreases for SSL6 and SSL10 which supports the change in charge compensation mechanism (see Eq. (5.2) and Eq. (5.5)). Similarly the tunnelling distance is found to decrease for sample SSL1 to SSL4 and thereafter, it gradually increased

for SSL6 and SSL10. The decrease in tunnelling distance increases the rate of electron hopping between Sn^{2+} and Sn^{4+} which results increase in the conductivity. The parameters obtained by fitting are in agreement with conductivity results as discussed above.

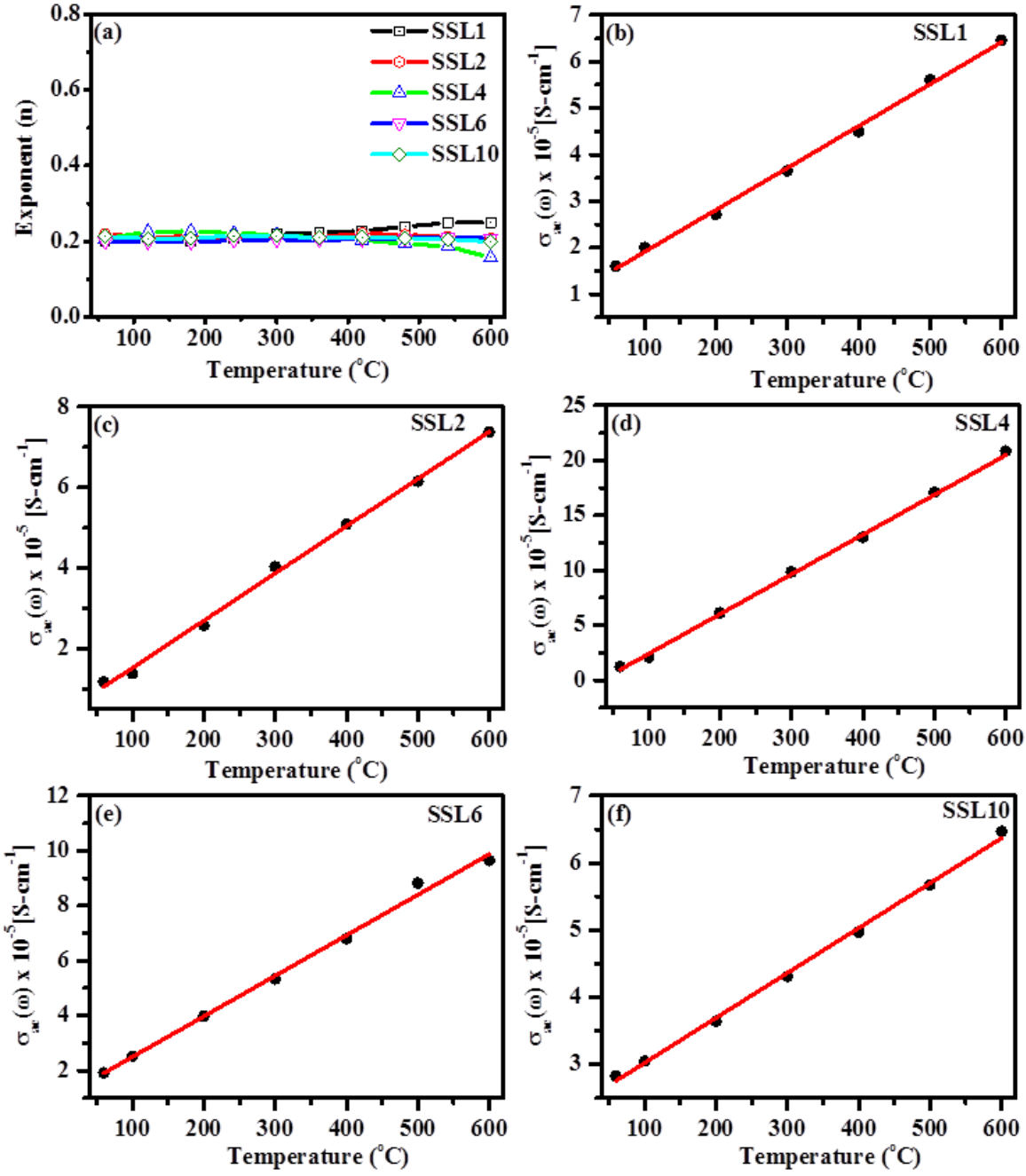

Figure 5.15 (a) Variation of power exponent, n with temperature (b)-(f) Variation of ac conductivity with temperature fitted with Eq. (3.11).

5.2.8.2 Modulus Spectroscopy analysis

Electric Modulus is considered to be powerful technique to study the relaxation process, [254]. Electric modulus data can be analysed in two form, (i) complex plane plot and (ii) spectroscopic plot. In this work, spectroscopic plots have been used to study the relaxation process [216].

The frequency variation of the real part (M') of the complex electric modulus (M^*) with logarithmic of frequency at different temperatures for a representative sample SSL4 is shown in Figure 5.16(a). At lower frequencies (< 10^3 Hz), the value of $M'(f)$ approaches zero, indicating the negligible contribution of sample-electrodes interface polarization. In mid frequency region (10^3 to 10^5 Hz) a dispersion in the value of M' is observed be due to presence of relaxation in the sample. Further, it is noticed that dispersion regions shifts towards higher frequency side with increasing temperature which indicates that relaxation process is temperature dependent. At higher frequency (> 10^5 Hz) M' shows a tendency of saturation at maximum asymptotic value which might be due to diminutive nature of forces governed by the mobile charge carrier under the presence of induced field [183, 217].

The frequency dependent variation of imaginary part of modulus $M''(f)$ at different temperatures for SSL4 is shown in Figure 5.16(b). The $M''(f)$ shows single broad peaks at characteristic frequency (f_{max}). Moreover, it is seen that position of peak (f_{max}) shifted towards higher frequency with increasing temperature. The width of peak $M''(f)$ observed in M'' vs. $\log f$ plots deals about the relaxation and conduction process occurring in the materials. The Kohlrauch - Williams - Watts (KWW) function given by Eq. (3.8) in Chapter 3 has been used to fit the imaginary part of modulus M'' in frequency domain [189]. The solid line shown in Figure 5.16(b) are data generated using Eq. (3.8) whereas symbols are experimental data of M''. The parameters M''_{max}, β and ω_{max} are extracted from the fitting. To study temperature dependent relaxation processes, relaxation frequency (f_{max}) are

obtained for all the samples and plotted the log $f_{max}\left(=\frac{\omega_{max}}{2\pi}\right)$ with inverse of temperature and shown in Figure 5.16(c). The linear variation of plot log f_{max} with 1000/T indicates that the relaxation process follow Arrhenius relation as given by Eq. (3.9). By linear fitting, value of activation energy ($E_{relax.}$), f_o are obtained. The value of $E_{relax.}, f_o, \tau_o\left(\frac{1}{f_o}\right)$ are given in Table 5.3 for all the samples. The activation energy for all samples falls in the range of (0.10±0.02 to 0.12±0.02) eV. The activation energy for relaxation ($E_{relax.}$) is almost same as the activation energy for conduction in the low temperature range. Therefore, relaxation mechanism is similar to conduction mechanism operative in region-1 and attributed to the hopping of electron between Sn^{2+} and Sn^{4+} sites. The range of activation energy for relaxation ($E_{relax.}$) is same as the activation energy for electron hopping in ferrites such as in between Fe^{2+}/Fe^{3+} or Ni^{2+}/Ni^{3+} [250, 251]. The values of β for all the sample is plotted with respect to temperature in Figure 5.16(d). The values of β falls in the range of 0.5-0.7 for all samples suggests that the relaxation processes are non-Debye type [183, 216].

Since, the investigated temperature and compositional ranges are wide thus possibility of change in relaxation mechanism can not be ruled out. In order to check whether relaxation mechanism is temperature dependent or independent, the imaginary part of modulus (M'') is scaled by M_{max} and frequency axis is scaled by f_{max} (obtained from fitting) for a sample SSL4 is shown in Figure 5.16(e). All the experimental data perfectly overlaps on a single master curve which suggest the validation of time-temperature superposition principle (TTSP). It also indicates that the relaxation mechanism remains same in whole temperature range. However, the scaled modulus spectra $\left(\frac{M''}{M''_{max}}\right)$ against frequency $\left(\frac{f}{f_{max}}\right)$ for all samples at 400°C is shown in Figure 5.16(f), which shows that with incorporation La the width of peak decreases and minimum for SSL4 and then increased for further increasing La concentration. Minimum width of M'' peak indicates that the distribution in relaxation time is

smaller in SSL4 sample, while nature of *M''* peak and position of maximum peak remains same for all sample further reconfirm that relaxation mechanism is invariant by La substitution.

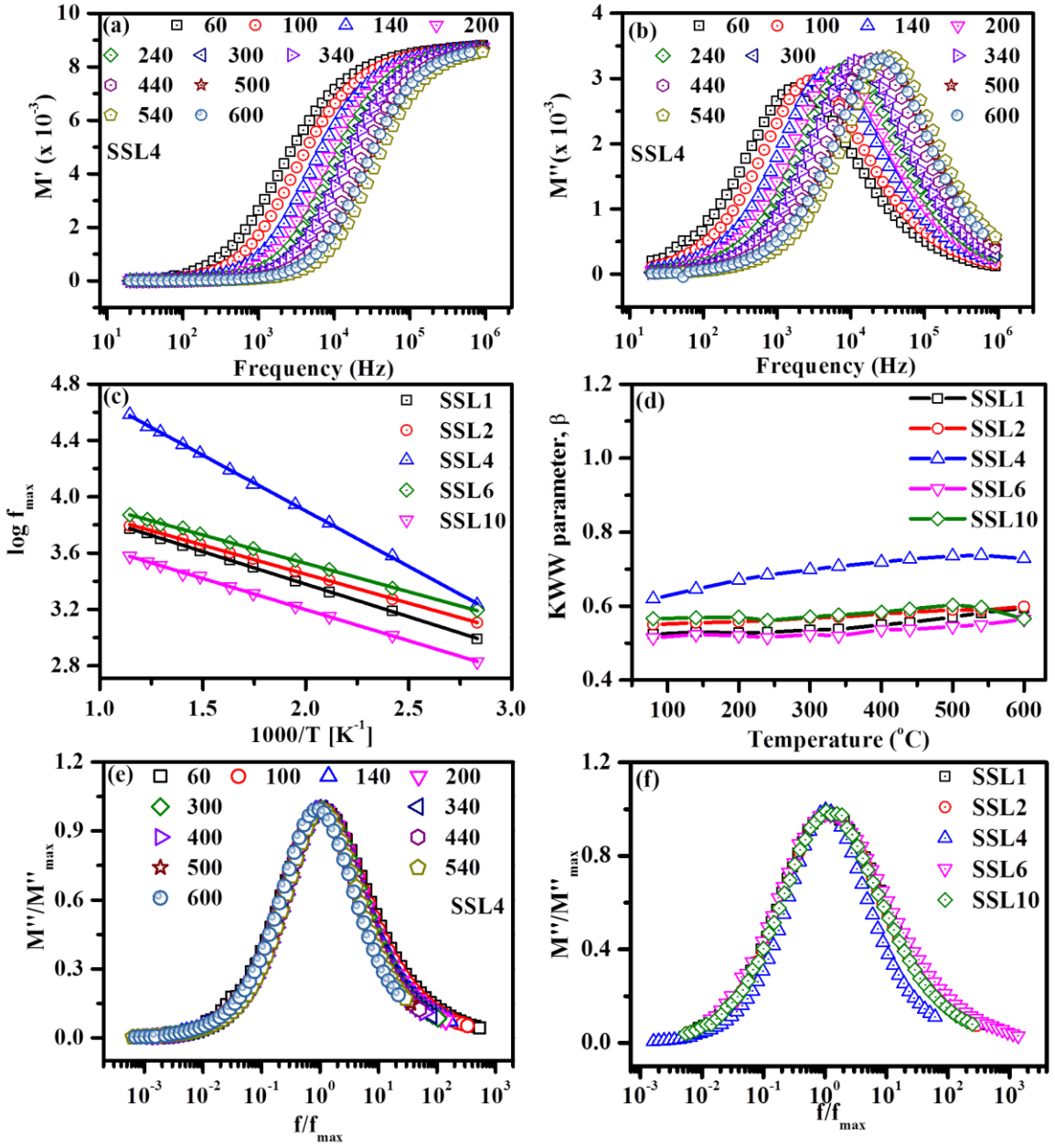

Figure 5.16 Variation of (a) Real part of modulus (*M'*) (b) Imaginary part of modulus (*M''*), with frequency at different temperatures (in ^{o}C) (c) Arrhenius plot for max. Frequency generated by Eq. (3.8) (d) KWW parameter, β with respect to temperature for all samples (e) Scaled Modulus vs. scaled frequency for sample SSL4 (f) Scaled Modulus vs. Scaled frequency for all samples at 400^{o}C.

Table 5.3 Activation energy for DC, AC and relaxation process, slope between dc conductivity and hopping frequency, relaxation frequency and relaxation time for all samples.

Parameters	**SSL1**	**SSL2**	**SSL4**	**SSL6**	**SSL10**
dc Activation Energy($E_{cond.}$)					
Region-1	0.50±0.02	0.47±0.02	0.23±0.01	0.50±0.02	0.43±0.02
Region-2	0.16±0.01	0.10±0.01	0.16±0.01	0.14±0.01	0.11±0.01
ac Activation Energy (E_{ac})					
Region-1	0.48±0.02	0.46±0.02	0.21±0.02	0.50±0.02	0.40±0.02
Region-2	0.14±0.01	0.15±0.01	0.14±0.01	0.16±0.01	0.12±0.01
Parameters obtained from QMT model					
α^{-1} (x 10^{-8})	(1.0013±0.0004)	(1.0102±0.0006)	(2.4423±0.0008)	(46.0152±0.0032)	(10.9823±0.0021)
$N(E_f)$ (x 10^{16})	5.3219±0.0001	5.3531±0.0001	57.1143±0.0087	1.2153±0.0001	2.8142±0.0001
R*w* (Å)	8.4279±0.0012	8.2273±0.0010	2.5573±0.0007	6.5762±0.0043	7.0410±0.0023
Activation Energy for Relaxation process ($E_{relax.}$)					
$E_{relax.}$	(0.11±0.02)	(0.12±0.002)	(0.10±0.02)	(0.12±0.02)	(0.11±0.02)
f_o	(2.03±0.01)x10^4	(1.88±0.01)x10^4	(3.01±0.01)x10^5	(1.21±0.01)x10^4	(2.15±0.01)x10^4
τo (x 10^{-5})	4.96±0.01	5.31±0.01	0.33±0.01	8.25±0.01	4.63±0.01

5.3 Conclusions

The single - phase powder of several system compositions $Sr_{2-x}La_xSnO_4$ (x = 0.01, 0.02, 0.04, 0.06 and 0.10) was successfully synthesized by calcining at 1000^{o}C for 8 hours using solid state reaction route. Rietveld refinement of XRD data shows that all the synthesized powder formed similar crystal structure and space group as undoped Sr_2SnO_4. The incorporation of La has been studied by Raman and Fourier's transformation of infrared (FTIR) spectroscopy, which reconfirm that synthesized powders are single phase. These studies showed that La solubility in Sr_2SnO_4 (10 % atoms) is higher than its perovskite component $SrSnO_3$ (2 % atoms). The optical band gaps of the samples have determined from absorption data using Tauc plot. The ac conductivity of the samples follows universal Johnscher's power law. Two regions of conduction are observed from dc conductivity and hopping frequency. Almost

similar value of activation energy obtained from dc conduction and hopping frequency shows similar process is operative in sample. In lower temperature range, conduction is governed by transfer of electron between Sn^{2+} and Sn^{4+}, while migration of interstitial oxygen takes place along a, b plane in higher temperature region. Sample SSL4 shows the highest conductivity among the all sample. Modulus spectroscopy plots are analyzed to study the relaxation process involved in the sample. KWW function is used to fit the spectroscopy plot of M'' vs. $\log f$ to determine the parameters M''_{max}, f_{max} and β for all sample in whole temperature range. Plot of $\log f_{max}$ with inverse of temperature suggests the Arrhenius type relaxation process operative in the sample. The value of activation energy E_{relax} is similar to the value of E_{cond} in region 2, which indicates that relaxation and conduction processes are similar in all sample and takes place by transfer of electron between Sn^{4+} and Sn^{2+}. The value of β lying in the range of 0.5-0.7 indicated that the relaxation processes are non-Debye type. Using UV absorption of materials as a metastable state it can be used for the application of UV detectors. It is also a promising candidate for electrical device and sensor applications due to electronic conduction at bulk level in the samples.